

Supplemental Table 1: Medical and neuropathological data of human donor eyes and brains.

Patient No.	Age [yrs], Gender, Ethnicity	Clinical Diagnosis [Duration (yrs); MMSE score]	Post-Mortem Neuropathology	Final Diagnosis [BRAAK]	Cause of Death
1	48, F, H	Dementia, AD [10 yrs] Probable Familial AD	Moderate to frequent NPs Moderate to frequent NFTs	AD definite	Cerebral atrophy with hydrocephalus
2	51, F, A	Familial Autosomal Dominant AD	Moderate to frequent NPs Frequent NFTs	AD definite, [V-VI]	–
3	63, F, C	Dementia, AD [16 yrs, MMSE: 9]	Frequent NPs Frequent NFTs	AD definite	–
4	64, F, C	Dementia, AD [MMSE: 5]	Sparse to moderate NPs Sparse to moderate NFTs	AD definite [VI]	–
5	65, F, C	Dementia, AD ² [5 yrs]	Moderate to frequent NPs Frequent NFTs	AD definite	–
6	69, M, N/A	Dementia, AD	Moderate to frequent NPs Frequent NFTs	AD definite	–
7	70, M, C	Dementia, AD [5 yrs]	Moderate NPs Moderate to frequent NFTs	AD definite	Pneumonia
8	71, M, C	Dementia, AD/FTD [12 yrs, MMSE: 10]	Moderate to frequent NPs Moderate to frequent NFTs	AD definite [VI]	–
9	79, M, C	Dementia, AD [10 yrs]	N/A	AD definite	Myocardial infarction
10	81, F, C	Dementia, AD [17 yrs, MMSE: 4]	Moderate to frequent NPs Frequent NFTs	AD definite [VI]	–
11	82, F, N/A	Dementia, AD	N/A	AD definite	–
12	83, M, C	Dementia, AD ² [10 yrs, MMSE: 15]	Moderate to frequent NPs Sparse to moderate NFTs	AD definite [IV]	–
13	83, M, C	Dementia, AD [7 yrs]	Moderate to frequent NPs Moderate NFTs	AD definite [VI]	–
14	85, M, C	Dementia, AD	N/A	AD definite	–
15	85, F, N/A	Dementia, AD	Moderate to frequent NPs Moderate to frequent NFTs	AD definite	–
16	87, M, B	Dementia, AD ² [8 yrs]	Moderate to frequent NPs Moderate NFTs	AD definite [V]	Cerebral infarction
17	88, M, C	Dementia, AD [3 yrs, MMSE: 4] (Occipital CVA ¹)	Moderate to frequent NPs Sparse to moderate NFTs	AD definite	Cerebral infarction
18	89, F, A	Dementia, AD [5 yrs, MMSE: 6]	Moderate to frequent NPs Moderate to frequent NFTs	AD definite [IV-V]	–
19	90, F, C	Dementia, AD [2 yrs, MMSE: 16]	Frequent NPs Frequent NFTs	AD definite	–
20	90, F, B	Dementia, AD ² [14 yrs]	Moderate to frequent NPs Frequent NFTs	AD definite	Cerebral hemorrhage infraction focal

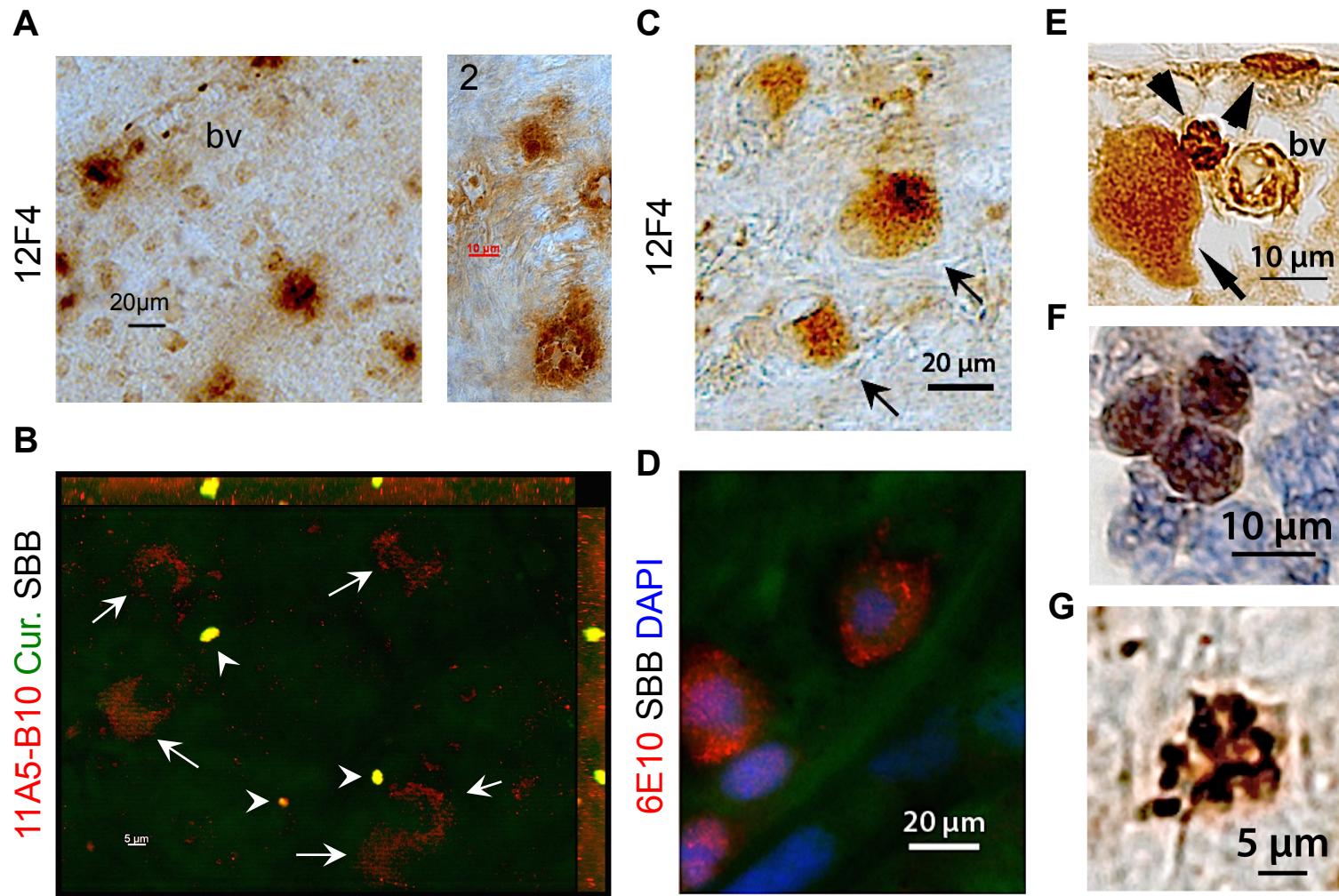
21	94, F, B	Dementia, AD ² [11 yrs]	Moderate to frequent NPs Frequent NFTs	AD definite [V – VI]	Cerebral infarction
22	97, F, C	Dementia, AD [10 yrs, MMSE: 4]	Sparse to frequent NPs Moderate to frequent NFTs	AD definite [V]	–
23	98, F, C	Dementia, AD [MMSE: 15]	Sparse to moderate NPs Sparse to moderate NFTs	AD definite [V]	–
AD	78.8 ±2.9 ^{ns} 14F/9M	Mean ±SEM (n=23)	F 78.4±4.5 ^{ns} M 79.4±2.5 ^{ns}		
24	58, M, B	Absence of Dementia	N/A	No AD Normal brain	Esophageal cancer
25	59, M, C	Absence of Dementia	N/A	No AD Normal brain	Acute myocardial infarction
26	64, F, C	Absence of Dementia	N/A	No AD Normal brain	Congestive heart failure
27	66, M, C	Absence of Dementia	N/A	No AD Normal brain	Liver failure
28	69, M, C	Absence of Dementia [MMSE: 28]	No DPs or NPs No NFTs	No AD Normal brain	–
29	70, F, N/A	Absence of Dementia	N/A	No AD Normal brain	–
30	74, M, C	Absence of Dementia	N/A	No AD Normal brain	Ruptured brain aneurysm
31	80, M, B	Absence of Dementia	N/A	No AD Normal brain	Pneumonia
32	83, M, C	Absence of Dementia [MMSE: 28]	Sparse to moderate NPs Sparse NFTs	No AD Normal brain	–
33	85, F, N/A	Absence of Dementia	N/A	No AD Normal brain	–
34	88, M, C	Absence of Dementia ²	Sparse to moderate NPs Sparse NFTs	No AD Normal brain	Cerebral infarction
35	91, F, C	Absence of Dementia [MMSE: 29]	Sparse to moderate NPs Sparse NFTs in neocortex	No AD [II]	Cancer
36	92, F, C	Absence of Dementia ² [MMSE: 25]	Sparse NPs; Moderate DPs Sparse NFTs in Hippocampus & Entorhinal cortex	No AD Normal brain	Cerebral infarction
37	95, F, C	Absence of Dementia	Sparse NPs No NFTs	No AD Normal brain	–
CTRLS	76.7 ±3.4 6F/8M	Mean ±SEM (n=14)	F 82.8 ±5.2 M 72.1 ±3.9		

AD - Alzheimer's disease; NPs - Neuritic plaques; DPs - Diffuse plaques; NFTs - Neurofibrillary tangles. Scoring: 0 = none; < 5 = Sparse; 6 – 20 = Moderate; 21 – 30 or above = Frequent. AD neuropathology was determined by Gallyas or Bielschowsky silver stain and Thioflavin S stain in hippocampus CA1, entorhinal cortex, mid frontal, sup/mid temporal, inferior parietal, primary visual and visual association area. Sample size: $n = 23$ confirmed AD patients and $n = 14$ controls. Definite AD is high probability of AD, according to the Consortium to Establish a Registry of Alzheimer's Disease (CERAD) criteria with NIA-Reagan criteria. Gender: F – Female; M – Male. Ethnicity: C – Caucasian; A – Asian; H – Hispanic; B – African American. MMSE - Mini-Mental State Examination. BRAAK - Braak stages [I - VI]. ¹CVA, cerebral vascular accident or stroke. ²A subset of human donors by which both brains and eyes were analyzed. N/A - not available. ^{ns} - ^{ns}No statistical difference between patients and control groups or females and males of each diagnostic group.

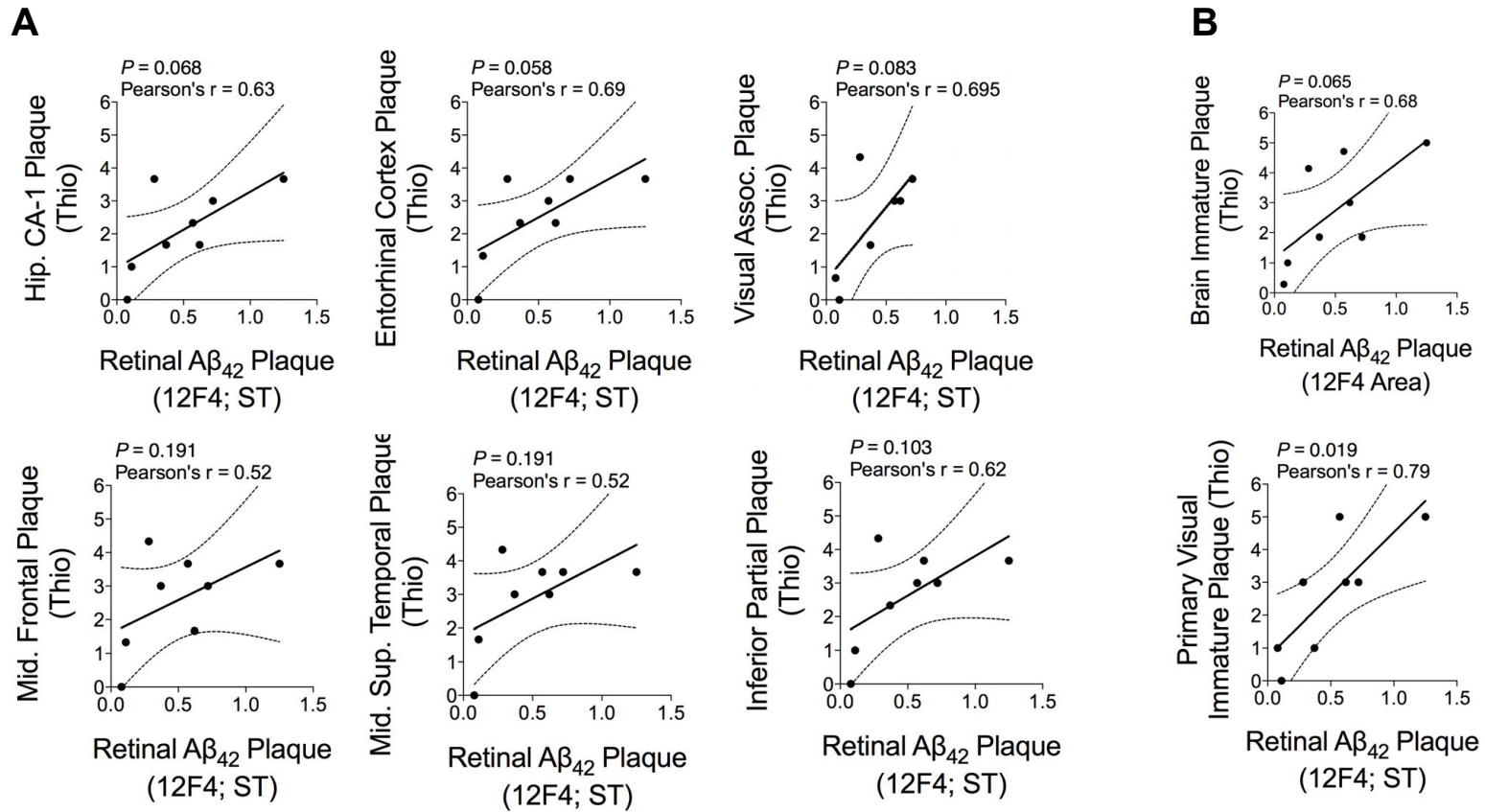
Supplemental Table 2. Human subjects enrolled in retinal amyloid imaging clinical study.

Patient ID	Age	Sex	Diagnosis	MMSE	RAI	Spot #
001 [≈]	63	M	Mild AD	22	73.7	71
002 [≈]	70	M	Mod AD	14	78.6	62
003 [≈]	72	M	Mod AD	19	85.3	36
004 [≈]	69	F	Mod AD	19	74.6	43
005 [≈]	69	F	Mod AD	19	43.9	17
006 [≈]	76	F	Mod AD	12	52.5	19
007	82	F	Mild AD	21	112.4	71
008	86	F	Mild AD	23	100.5	82
009	86	F	Mild AD	23	107.0	65
010	87	F	Mild AD	23	60.8	36
<i>Mean ±SEM (Subgroup[≈])</i>	<i>76 ±2.7[*] (69.8 ±1.7)^{ns}</i>	<i>3M, 7F (3M, 3F)</i>	<i>AD Dementia</i>	<i>19.5 ±1.2 (17.5 ±1.5)</i>	<i>78.9 ±7.2^{***} (74.4 ±8.4)^{**}</i>	<i>50.2 ±7.3[*] (41.3 ±8.9)^{ns}</i>
011	21	M	CTRL	N/A [∅]	18.4	36
012 [≈]	50	M	CTRL	N/A [∅]	46.3	43
013 [≈]	49	F	CTRL	N/A [∅]	25.7	28
014 [≈]	53	F	CTRL	N/A [∅]	23.4	02
015 [≈]	69	F	CTRL	N/A [∅]	21.0	28
016 [≈]	75	F	CTRL	N/A [∅]	46.1	12
<i>Mean ±SEM (Subgroup[≈])</i>	<i>53 ±7.7 (59.2 ±5.4)</i>	<i>2M, 4F (1M, 4F)</i>	<i>CTRL</i>	<i>N/A[∅]</i>	<i>30.2 ±5.2 (32.5 ±5.6)</i>	<i>24.8 ±6.2 (22.6 ±7.1)</i>

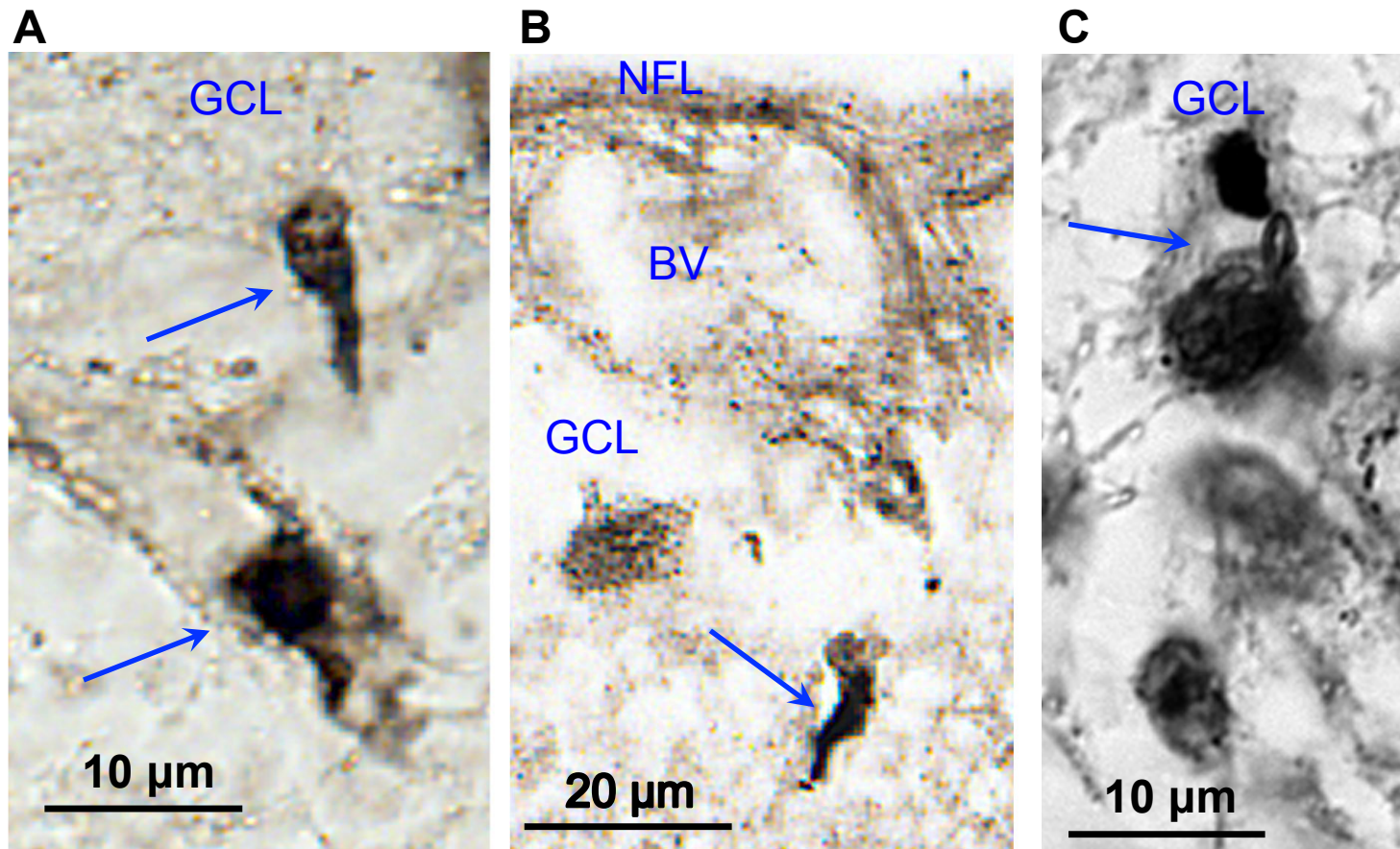
Mod AD – moderate AD. CTRL – healthy controls. N/A[∅] – MMSE not available; asymptomatic individuals with no evidence for memory or cognitive executive impairment according to self-reporting and/or family members. These individuals exhibit no deficit in activity of daily living (ADL). [≈] A subgroup of 6 AD and 5 CTRL subjects, where mean ages of groups AD vs. CTRL is not statistically different. ^{ns} No statistical difference. ^{*}*P*<0.05, mean age or retinal plaque # in all AD vs. CTRL subjects (2-tail ttest). ^{**}*P*<0.005, RAI scores of age-selected subgroup[≈] of AD vs. CTRL subjects (2-tail ttest). ^{***}*P*<0.0005, RAI scores of all (non age-matched) 10 AD vs. 6 CTRL subjects (2-tail t-test).



Supplemental Figure 1. Extra- and intra-cellular A β deposits found in retinal flatmounts and cross sections isolated from definite AD patients. A. Distribution of extra- and intra-cellular 12F4⁺ A β ₄₂-containing deposits (with peroxidase-DAB labeling), abluminal and along blood vessels (bv) in flatmount retinas of AD patients. **B.** Fluorescent labeling of flatmount retinas with curcumin (Cur.; green) and anti-A β ₄₀ 11A5-B11 mAb (red) indicates both cytoplasmic A β (arrows) and extracellular A β deposits (arrowheads point to yellow spots representing Cur and 11A5-B11 co-labeling). High magnification images showing cytoplasmic 12F4⁺ (**C**) and 6E10⁺ (**D**) A β immunoreactivity in retinal flatmounts from AD patients. DAPI stains nuclei. Sudan black B (SSB) is used to quench non-specific auto-fluorescent signals. **E-G.** Retinal cross-sections stained with 12F4 and DAB, with **F.** including hematoxylin staining.



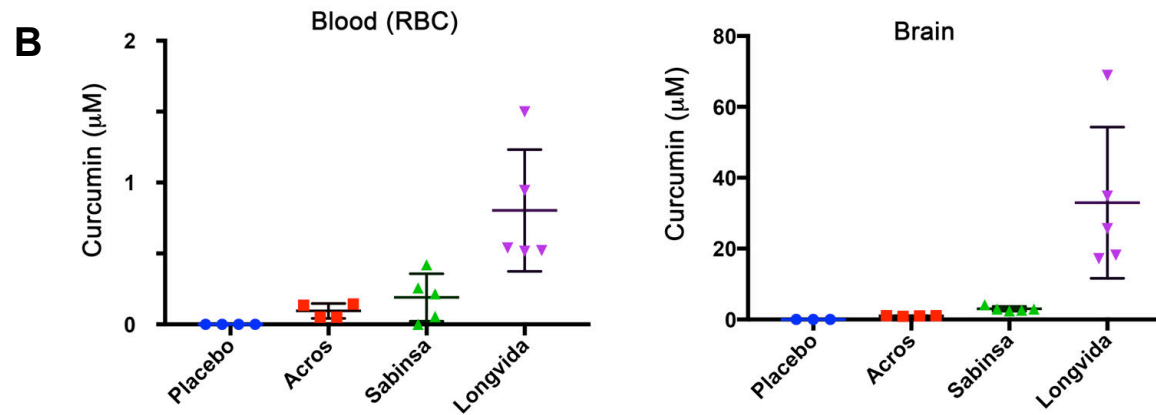
Supplemental Figure 2. Correlation analyses between retinal $A\beta_{42}$ plaques in the superior temporal region and cerebral plaques in various brain regions. A. Multiple correlation analyses between retinal $A\beta_{42}$ -containing deposits (area) in the superior temporal quadrant (ST) and cerebral plaques stained with Thioflavin-S (Thio) in various regions, including hippocampal *Cornu Ammonis-1* (Hipp. CA-1), entorhinal cortex, visual association cortex, middle frontal gyrus/cortex, middle superior temporal gyrus, and inferior parietal cortex. **B.** Correlation analysis between immature-type Thio⁺ plaques for all brain regions (as above, plus the primary visual cortex) and retinal $A\beta_{42}$ plaque area in ST (upper graph). A significant positive association is found between retinal $A\beta_{42}$ plaque and immature plaque burden in the primary visual cortex (lower graph). Statistical analyses were performed utilizing the Pearson's correlation coefficient (r) test in a subset of AD patients and matched controls (n=8). Significance is presented as a P value.



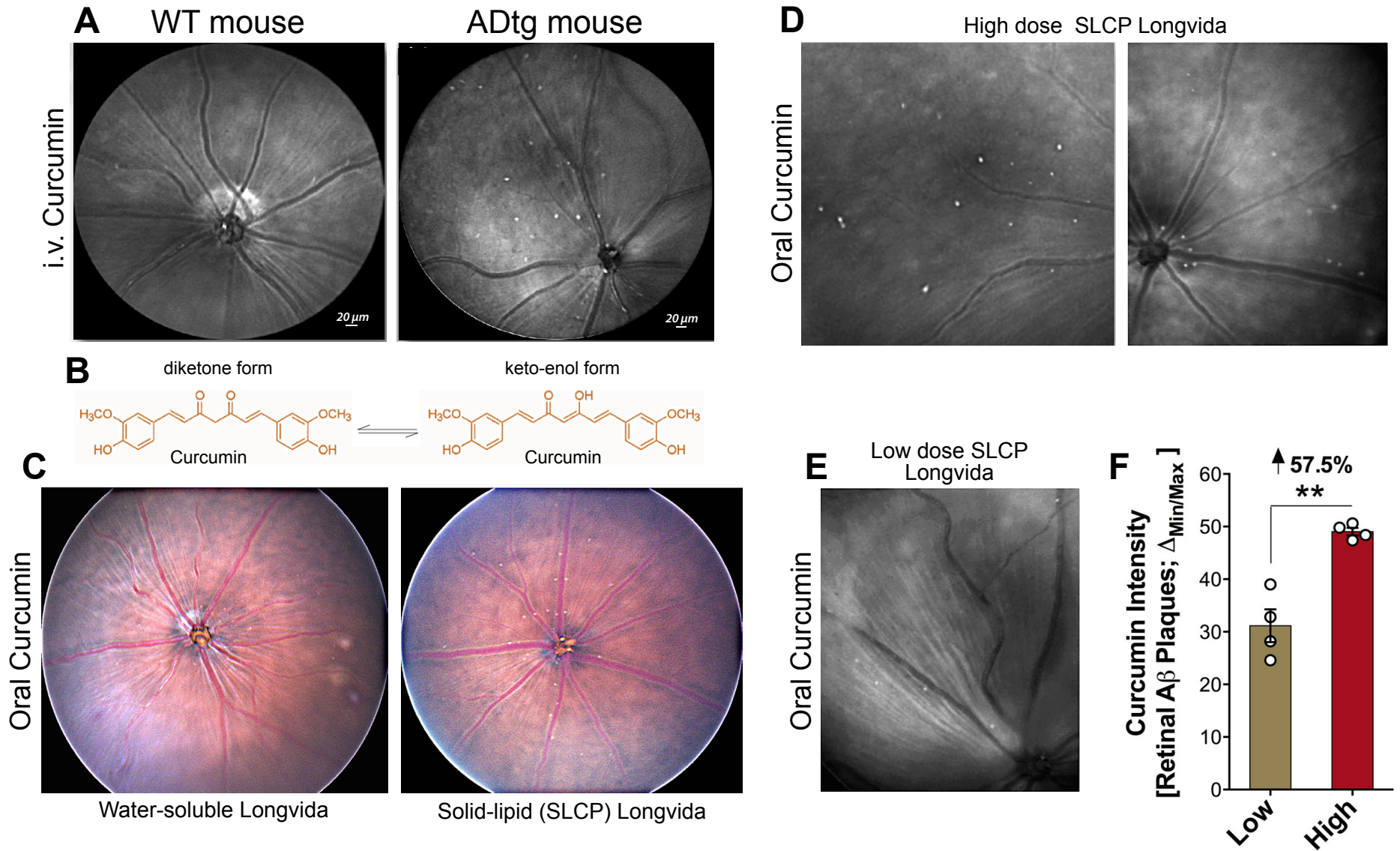
Supplemental Figure 3. Neurofibrillary tangles (NFTs)-like structures in retinal cross sections of definite AD patients. A-C. Gallyas silver staining of retinal cross sections isolated from neuropathologically confirmed AD patients shows intraneuronal positive staining resembling NFTs, especially in the retinal ganglion cell layer (GCL, marked in blue arrows).

A Effect of different commercial sources of curcumin on blood and brain levels in mice fed curcumin in chow for 2 weeks

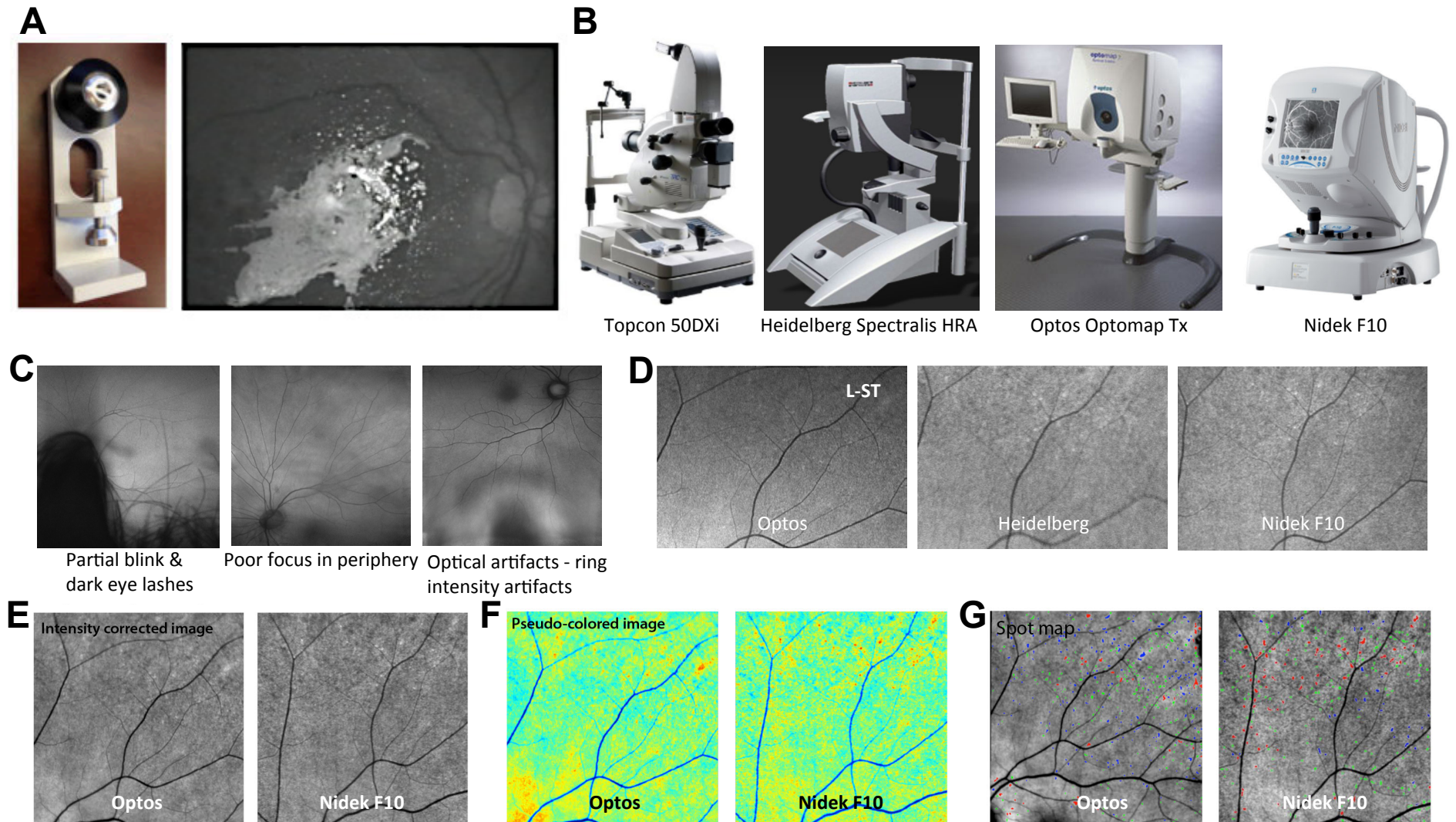
Curcumin Source	RBC Curc (μM)	Brain Curc ($\mu\text{g/g t}$)	Brain Curc (μM)	Brain/RBC ratio
Vehicle	ND	ND	ND	N/A
Longvida	$0.803 \pm 0.429^*$	$12.120 \pm 7.847^*$	32.940 ± 19.014	41.02
Sabinsa	0.190 ± 0.167	$1.114 \pm 0.242^*$	3.028 ± 0.631	15.93
Acros	0.110 ± 0.052	$0.382 \pm 0.028^*$	1.039 ± 0.095	9.44



Supplemental Figure 4. Differences in bioavailability between commercial formulations in adult mice fed equivalent amounts of curcumin (2000 parts per million in chow). Three different commercial formulations of curcumin were fed to wild type mice (C57BL/6; n=3-5 per group) ad libitum for 14 days. Mice were then euthanized, and blood samples and brains were collected and stored at -80°C for further analysis. Blood was collected in EDTA tubes, separated into red blood cell (RBC) and plasma fractions, and snap frozen in dry ice. After thawing and in preparation for measurement of curcumin levels, acetic acid was added to blood samples prior to ethylene acetate extraction to limit curcumin degradation. Curcumin was then measured using high-performance liquid chromatography (HPLC). **A.** The table shows group means and standard deviations of RBC and brain levels [grams wet tissue (g t) or mM]. ND, not detectable; N/A, not applicable. Asterisks signify differences between source curcumin (within tissue compartment). * $p < 0.05$, one-way ANOVA. Note that concentrations in the brain are at least 9 times higher than in the blood. **B.** The scattergram plots show individual values, means and standard deviation in RBC and brain tissue.



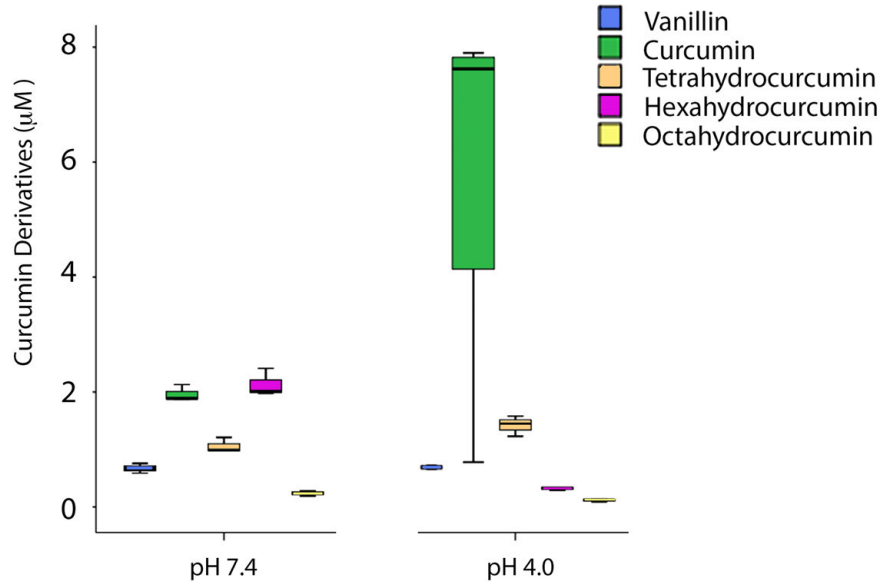
Supplemental Figure 5. Curcumin optimization for in vivo retinal amyloid imaging in double-transgenic APP_{SWE}/PS1_{ΔE9} (ADtg) mouse models. Administration regimen (route, dosage, frequency) and different types of curcumin formulations were tested for noninvasive retinal amyloid imaging. **A.** Representative fundus retinal images capturing specific curcumin fluorescence bound to Aβ deposits following an intravenous (i.v.) injection of curcumin (Sigma-Aldrich; 7.5 mg/Kg once a day for 2 days). **B.** Curcumin tautomeric forms. **C.** Fundus bright-field images of live ADtg mouse retinas after oral administration of water soluble or non-water soluble proprietary SLCP (Solid lipid curcumin particle) Longvida (optimized curcumin). **D-E.** Increased fluorescent signal of retinal Aβ deposits following high-dose (**D**) vs. low-dose (**E**) SLCP Longvida. **F.** Quantitative analysis showing increased mean curcumin-labeled plaque intensity fluorescent signals following high- vs. low-dose curcumin oral administration. Five plaques per image were analyzed for each mouse (n=4 mice per group) using ImageJ delta Min/Max ROI values. Mean ± SEM are shown. *** $P = 0.0014$ by two-tailed unpaired t-test.



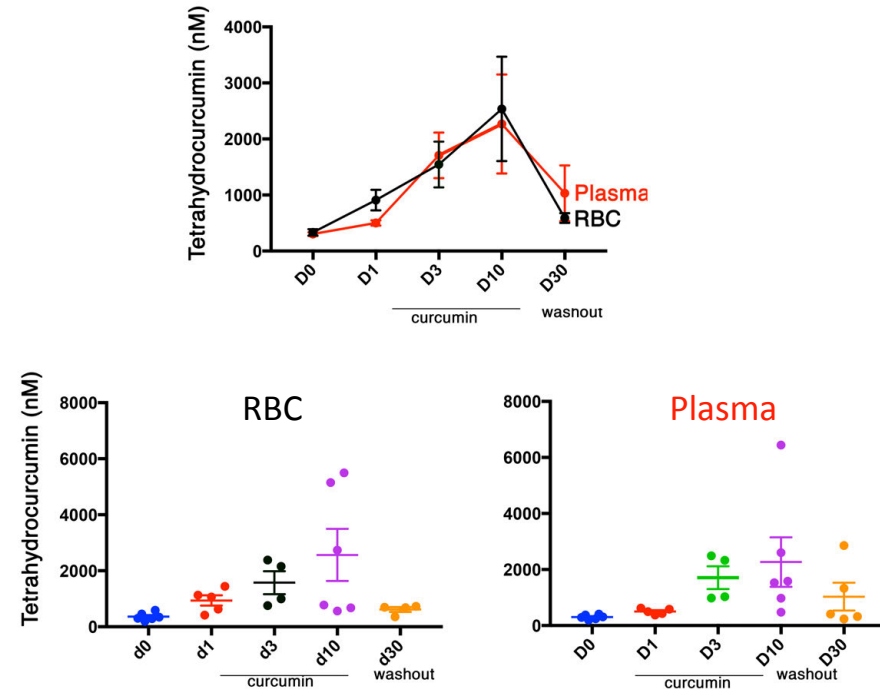
Supplemental Figure 6. Calibration and testing of ophthalmic devices for clinical trials. **A.** A model eye was developed to provide a standardized means of comparison between retinal imaging devices, and to test device modifications and improvements. The model eye is the optical equivalent of a live human eye, but is retrofitted with various targets representing the retina. The right image shows an adaptation consisting of fluorescent micro-beads with a peak fluorescence at 605nm (based on curcumin emission peak). **B.** Utilizing various modified ophthalmoscopes fitted for human in vivo curcumin-amyloid imaging: calibration, modification, and testing in live patients. **C.** Examples of data exclusion criteria. **D-G.** In vivo curcumin fluorescence imaging in an AD patient at the same retinal location (L-ST - left eye, superior temporal). **D.** Different excitation wavelengths (488nm, 532nm). **E-G.** A representative comparison between two modified ophthalmic devices (Optos vs. Nidek) used in the clinical trials, showing image processing, threshold and spot map definition (red spots mark increased curcumin fluorescence vs. the Baseline image).

A

Acidic pH protects curcumin (11 μM) and limits curcumin degradation in human blood ex vivo (2 hr at 37°C)

**B**

Curcumin reduction by blood tetrahydrocurcumin levels (see Fig 6E for curcumin levels)

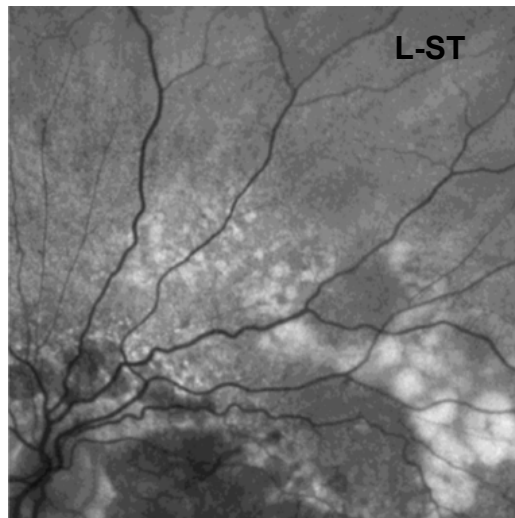
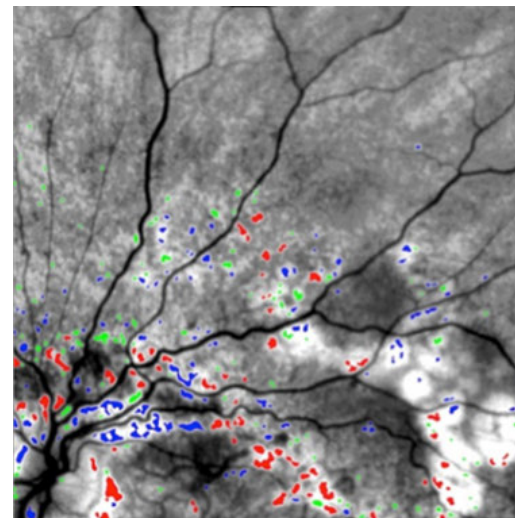


Supplemental Figure 7. Degradation or reduction of curcumin in human blood ex vivo and in vivo. **A.** Data show that acidification of blood is critical to attenuate ex vivo reduction and degradation of curcumin metabolites compared to neutral pH. To evaluate the impact of temperature and pH on degradation of curcumin in human blood, blood samples ($n=3$) were spiked with 11 μM curcumin and incubated for 2 hours at 37°C ex vivo at neutral or acidic pH, and curcumin and its metabolites were measured using LC/MS/MS. Concentrations were calculated based on peak areas of the following mass ion transitions: ferulic acid, 193>133 m/z ; 193>178 m/z ; vanillin, 152>136.4; octahydrocurcumin, 376>122.2 m/z and 376>134.9; hexahydrocurcumin, 374>179.1 m/z , 374>193.1 m/z ; tetrahydrocurcumin, 372>193.5 m/z ; 372>236 m/z ; curcumin, 367>148.7 m/z ; 367>172.4 m/z ; 367>216.3 and the Internal Standard tetramethoxycurcumin, 396.4>149.5 m/z , 396.4>297.1 m/z ; 396.4>311.6 m/z and 396.4>337.6 m/z . **B.** Data show tetrahydrocurcumin levels in living healthy controls ($n=4-6$ subjects per time point) after intake of curcumin for 10 days (curcumin levels are depicted in Fig 6E). The top graph shows the mean levels \pm SD in red blood cells (RBC) and plasma, and the bottom graphs show scatterplots of the RBC and plasma data \pm SEM. Tetrahydrocurcumin levels are several-fold higher than curcumin, demonstrating reduction of curcumin, which likely occurs in vivo and ex vivo.

A

Patient ID	Age (y)	Sex	Diagnosis	MMSE
017*	68	Male	Dry AMD	30
018	74	Female	Dry AMD	30

*Retinal curcumin image provided. Mini Mental State Examination (MMSE)

B**C**

Supplemental Figure 8. Retinal curcumin imaging in live subjects with dry age-related macular degeneration (AMD). Two cognitively normal (non-AD) subjects with dry AMD were imaged following a 2-day curcumin intake protocol. **A.** Table of human subject details. **B.** A representative baseline image from the L-ST region (left eye, superior temporal) prior to curcumin intake (baseline). **C.** Image captured following curcumin intake, processed with defined threshold (spot map; red spots mark increased fluorescence after curcumin intake vs. baseline image). Densely fluorescent structures associated with drusen and typical maculopathy are shown in the posterior pole and central retinal regions.

Supplemental Data

Retinal amyloid pathology and proof-of-concept imaging trial in Alzheimer's disease

Yosef Koronyo¹, David Biggs², Ernesto Barron³, David S. Boyer⁴, Joel A. Pearlman⁵, William J. Au⁶, Shawn J. Kile⁶, Austin Blanco², Dieu-Trang Fuchs¹, Adeel Ashfaq⁷, Sally Frautschy⁸, Gregory M. Cole⁸, Carol A. Miller⁹, David R. Hinton¹⁰, Steven R. Verdooner², Keith L. Black¹, Maya Koronyo-Hamaoui^{1,11∞}

¹Department of Neurosurgery, the Maxine Dunitz Neurosurgical Research Institute, Cedars-Sinai Medical Center, Los Angeles, CA, USA; ²NeuroVision Imaging (NVI), LLC, Sacramento, CA, USA; ³The Doheny Eye Institute, Los Angeles, CA, USA; ⁴Retina Vitreous Associates Medical Group, Beverly Hills, CA; ⁵Retinal Consultants Medical Group, Sacramento, CA; ⁶Sutter Neuroscience Institute, Sacramento, CA; ⁷David Geffen School of Medicine, University of California Los Angeles, CA, USA; ⁸Departments of Neurology and Medicine, University of California Los Angeles; Geriatric Research Education and Clinical Center; Veterans Greater Los Angeles Healthcare System; Los Angeles, CA; ⁹Department of Pathology Program in Neuroscience, Keck School of Medicine, University of Southern California, Los Angeles, CA; ¹⁰Departments of Pathology and Ophthalmology, USC Roski Eye Institute, Keck School of Medicine, University of Southern California, Los Angeles, CA; ¹¹Department of Biomedical Sciences, Cedars-Sinai Medical Center, Los Angeles, California, USA.

[∞]**Corresponding Author:** Maya Koronyo-Hamaoui, PhD, Cedars-Sinai Medical Center, 127 S. San Vicente Blvd., Los Angeles, CA, USA 90048. Tel: (310)-423-7473, E-mail: maya.koronyo@cshs.org

Extended Methods

Postmortem eyes and brains. Human tissues were obtained from the Alzheimer's Disease Research Center (ADRC) Neuropathology Core (IRB protocol: HS-042071) at the University of Southern California's (USC; Los Angeles, CA) Department of Pathology. Postmortem specimens (Supplemental Table 1) were collected from 23 clinically and neuropathologically confirmed AD patients (mean age \pm SEM: 78.8 \pm 2.9; range 48-98 years; 14 females and 9 males with different disease severities) and from 14 age-matched healthy controls (mean age \pm SEM: 76.7 \pm 3.4; range: 58-95 years; 6 females and 8 males, showing neither dementia nor brain pathology). The groups did not differ significantly in age.

Clinical and neuropathological assessment of human tissues. The clinical and neuropathological reports included neurological examinations and neuropsychological tests, providing data on cognition, family history, and medication. Reports were provided by the USC ADRC Clinical Core (IRB protocol: HS-042071). A trained psychometrist tested each participant individually, under supervision of a licensed clinical neuropsychologist. Test scores from evaluations performed closest to death were used in this analysis. Most cognitive evaluations were performed annually, and, in most cases, less than one year prior to death. Two global indicators of cognitive status were used for clinical assessment, the Clinical Dementia Rating (CDR) and the Mini Mental State Examination (MMSE, normal cognition = 24-30; MCI = 20-23; moderate dementia = 10-19; severe dementia \leq 9). For neuropathological diagnoses, the modified Consortium to Establish a Registry for Alzheimer's Disease (CERAD)(1) was used as outlined in the National Institute on Aging (NIA)/Regan protocols with revision by the NIA and Alzheimer's Association(2). These included A β burden and NFT pathology assessments in multiple brain areas. Amyloid plaques and tangles in the brain were evaluated using the Thioflavin-S (Thio) fluorescent and Gallyas silver stains in formalin-fixed, paraffin-embedded tissues. Three neuropathologists provided scores based on independent observations of amyloid or NFT burden (0=none, 1=sparse, 3=moderate, 5=abundant), and an average of all three readings was assigned to each individual. Braak scores were

used to assess NFTs for disease progression. Neuronal loss and gliosis were evaluated in multiple brain areas using haematoxylin and eosin (H&E) stain.

Preparation of retinal and cortical tissues. Donor eyes were collected within 6 hours from time of death and were either preserved in Optisol media (stored at 4°C for short-term), fresh frozen (snap; stored at -80°C for long-term), or punctured and fixed in 10% neutral buffered formalin (NBF; long-term storage at room temperature). In addition, brains (frontal cortex tissues) from the same patients and several eyes were snap frozen and stored at -80°C. The immunostaining appeared homogenous across the three preparation methods, except for the DAPI staining, which was clearer in eyes that were snap frozen or preserved in Optisol without long-term NBF fixation. Fresh-frozen brains were cryosectioned (30µm thick), fixed with 2.5% PFA (paraformaldehyde) for 48 h, and placed in 1X PBS with 0.01% sodium azide (Sigma-Aldrich) at 4°C.

Retinal Flatmounts. Fresh-frozen eyes and eyes in Optisol were dissected with anterior chambers removed to create eyecups. Vitreous humour was thoroughly removed manually and the eyecups were hyaluronidase-treated (type I-S; Sigma-Aldrich) to liquefy and remove the vitreous humour remains. Then, eyecups were washed with PBS and fixed in 2.5% PFA for 2 days. Retinas were dissected out, detached from the choroid, and flatmounts were prepared. Alternatively, long-term NBF-fixed eyes were dissected to create eyecups, washed in PBS, and the retinas were dissected free.

Retinal cross-sections. Flatmounts were initially embedded in paraffin using standard techniques and were cut (7-10µm thick) vertically, from the center to the rim of the retina. Before immunohistochemistry, the sections were deparaffinized twice with 100% xylene for 10 minutes, rehydrated with decreasing concentration of ethanol (100% to 70%), and then washed with distilled water followed by PBS. Twenty of the 37 human retinal AD and control samples were cross-sectioned. Cross-

sections from each individual were investigated in parallel utilizing various staining approaches as specified below.

A β immunohistochemistry. Brains, retinal cross-sections, and retinal flatmounts were washed in PBS, then treated with target retrieval solution at 97°C for 1 hour (pH 6.1; Dako #S1699) and washed with PBS. For peroxidase-based immunostaining, tissues were washed in PBS, treated with 3% hydrogen peroxide for 12 min, and washed again in PBS. Thereafter, retinas were immunostained according to manufacturer specification using a Vectastain Elite ABC Kit (Vector Laboratories, USA #PK-6102), a highly sensitive avidin/biotin-based peroxidase enzyme system. Briefly, tissues were first treated with blocking solution and permeabilized with 0.1% Triton® X-100 (Sigma #T8787) for 30 min at room temperature before incubation with primary mouse anti-human A β mAb clones 6E10 or 12F4 (recognizing the 1-16aa N-terminal or the 42aa C-terminal, correspondingly; 1:150 in PBS with 10% permeabilization/blocking solution; Biolegend #803001 or #805502) for 72 h (flatmounts) or 16 h (cross-sections) at 4°C. Next, A β immunoreactivity was detected with a high-sensitivity immunoperoxidase method using 3,3'-diaminobenzidine (DAB) plus Substrate Chromogen System (Dako #K3467). Then, the nuclei were stained with a standard haematoxylin staining technique and the tissues were mounted (Dako #S3025). Bright-field images were acquired using a Carl Zeiss Axio Imager Z1 fluorescence microscope (Carl Zeiss MicroImaging, Inc.) equipped with ApoTome, AxioCam MRm and AxioCam HRc cameras. Images were repeatedly captured at several focal planes throughout the tissue.

For fluorescent-based immunostaining, tissues were washed in PBS and treated with antigen retrieval solution, as described above. Next, tissues were washed again in PBS and blocked for 1 hr with 20% donkey serum and 0.1% Triton® X-100. The tissues were incubated for 72 h (flatmounts) or 16 h (cross-sections) at 4°C with PBS containing 10% blocking solution, primary mAbs (mouse anti-human A β clone 6E10 or 12F4, as described above), 11A50-B10 (Biolegend: #805401), or 4G8 (Biolegend #800701) reactive to C- or N-terminal amino acid residues of A β (1:150 in PBS with 10%

permeabilization/blocking solution). Secondary polyclonal donkey anti-mouse Abs (1:200; Jackson ImmunoResearch Laboratories) conjugated with Cy-2 (#715-225-151), Cy-3 (#715-165-151), Cy-5 (#715-175-151) or DyLight™ 649 (#715-495-151) were incubated for 1 hr at 37°C. For tissues co-stained with curcumin, the curcumin staining was performed following the secondary Abs and the staining with Sudan Black B (SBB; Sigma-Aldrich #199664), when the latter was applied to the staining procedure. SBB (C₂₆H₂₄N₄O) is a lysochrome used for staining neutral triglycerides and lipids to eliminate background fluorescence. Tissues were then washed in PBS and mounted with media containing DAPI (Prolong®, Molecular Probes). Images were repeatedly captured at several focal planes using the same fluorescence microscope described above. In both staining techniques, routine controls were processed using identical protocols, while omitting the primary antibody to assess nonspecific labeling.

Aβ plaque distribution analysis. The geographical location of 12F4-positive Aβ plaques was determined by examining large regions within each quadrant of retinal flatmount. The layer distribution of these deposits was determined by screening radial cross-sections spanning the ora serrata to the optic disc, prepared from superior-temporal and inferior-nasal retinal quadrants. About 10 cross-sections were analyzed per patient at 10 μm intervals to assess retinal layer distribution. Images were captured at either 20x or 40x objectives, at respective resolutions of 0.5 and 0.25 μm covering central, mid, and far peripheral regions at a depth of 50 μm.

Retinal Aβ₄₂ plaque quantification. 12F4-positive Aβ plaques were analyzed following peroxidase-based immunostaining, from retinal superior temporal (ST) quadrants of 8 AD patients (mean age ±SEM: 74.25 ±5.28; 4 females and 4 males) and from 7 age-matched healthy controls (mean age ±SEM: 74.0 ±5.46; 3 females and 4 males). Images were captured at 20x objective, covering the entire ST quadrant. Images were exported to ImageJ 1.46r (NIH program) to calculate 12F4-positive Aβ plaques total area.

Brain plaques quantification. The ADRC neuropathological reports provided comprehensive data on cerebral diffuse, immature (neuritic, no core), and mature (neuritic, with core) A β plaques, stained with Thioflavin-S. Neuritic A β plaques, with or without cores, were determined by Gallyas silver stain. The cerebral A β plaques were examined from seven brain regions, including: hippocampal Cornu Ammonis-1 (Hipp. CA-1), entorhinal cortex, middle frontal gyrus/cortex, middle superior temporal gyrus, inferior parietal cortex, primary visual cortex and visual association cortex. The severity of cerebral A β burden was calculated as: 0=None; 1=sparse (>5 plaques); 3=moderate (6-20 plaques); 5=Frequent (21-30 plaques or above); or N/A= Not applicable. Average of burden scores was calculated for each brain region separately, for total brain regions (Brain), and for each type of plaque (diffuse, immature and mature).

Curcumin and Sudan Black B staining. Curcumin solution was prepared by dissolving 2 mg curcumin (Sigma-Aldrich #C1386) or (Longvida® Solid-Lipid Curcumin Particle) in two drops of 0.5M NaOH, mixing vigorously with a vortex, and immediately dissolving and diluting in PBS to achieve a final concentration of 0.1mg/ml or 0.2mg/ml for curcumin with final pH = 7.9. Human retina and brain sections and retina flatmounts were initially treated with 0.3% (w/v) Sudan Black B (Sigma-Aldrich #199664) in 70% ethanol (v/v) for 10 min at room temperature. All human tissues were stained with curcumin solution for 10 minutes at room temperature, and then washed three times with PBS for 15 minutes each. The samples were covered with ProLong™ Gold antifade mounting media with DAPI (Molecular Probes #P36935) or Vectashield (Vector Laboratories, Inc.) with (#H-1200) or without (#H-1000) DAPI.

Nissl staining and quantification. Paraffin-embedded sections were deparaffinized and rehydrated as described above. Sections were stained in 0.1% Cresyl Violet acetate (Sigma #C5042) for 5 min, rapidly rinsed in tap water, and briefly dipped in 70% ethanol. The sections were then dehydrated through 2x changes of absolute ethanol for 3 min each, then immersed in xylene 2x for 2 min and mounted in mounting medium xylene (Fisher scientific company, L.L.C #245-691). Nissl-stained retinal cross

sections (from the superior quadrant) were analyzed to quantify area and numbers of retinal neurons from 9 AD patients (mean age \pm SEM: 80.33 \pm 3.32; 5 females and 4 males) and from 8 age-matched healthy controls (mean age \pm SEM: 77.25 \pm 4.50; 5 females and 4 males). Twelve images were captured at 20x objective, covering the retinal neurons from the optic disc to the ora serrata. Images were exported to ImageJ 1.46r (NIH program) to calculate retinal neurons numbers and area.

Gallyas silver staining. Gallyas silver stain was used to detect neuritic plaques, neuropil threads (abnormal neurites), and neurofibrillary tangles. This is a standard method for staining neurofibrillary tangles associated with AD, which contain the 3 and 4 tandem repeats of the fibril tau isoforms of the microtubule binding regions of tau(3, 4). Briefly, tissues were deparaffinized and rehydrated in distilled water before immersion in 5% periodic acid (Sigma #P7875) for 5 min, and then in distilled water. Sections were placed in silver iodide solution containing distilled water, sodium hydroxide, potassium iodide, and 1% silver nitrate (Sigma respectively #S5881, #60399, and #209139) for 1 min, and then in 0.5% acetic acid (Fisher chemicals #BP2401) followed by rinse in distilled water. Next, the sections were placed in a fresh developer solution containing distilled water, sodium carbonate, ammonium nitrate, silver nitrate, tungstosilicic acid, and 37% formaldehyde (Sigma respectively #451614, #221244, #209139, #383341, and #F8775), until the sections turned a pale brown/gray color. The developer reaction was blocked by 0.5% acetic acid. Subsequently, sections were dehydrated in ethanol and xylene then covered with cyto seal 60 (Thermo Scientific #8310-4).

Congo red amyloid staining of Toluidine blue stained flatmount retinas. In order to stain the previously stained and mounted whole retinas with Congo red, affixed coverslips are first removed, then slides are immersed in 100% Xylene for 3 to 5 days. Next, flatmount retina slides are placed in 3 one-minute changes of 100% ethanol, followed by 3 one-minute changes in 95% ethanol, and rinsed in running water for 1 min. Slides are then dipped in Congo Red Amyloid Stain (American MasterTech Inc., Lodi California) for 60 min at room temperature before treatment with a 1% sodium hydroxide solution 3 times

for 15 seconds, followed by a one-minute rinse in running tap water. Finally, slides are dehydrated, covered with mounting media and coverslips. Slides were imaged at 20x with a bright field Olympus (Center Valley, PA) BH2 microscope equipped with a polarizer and analyzer for detecting birefringence. Images were photographed with a Spot II digital camera (Diagnostic Instruments, Sterling Heights, MI).

Transmission electron microscopy. Retinal flatmounts were washed in PBS, then treated with target retrieval solution at 97°C for 1 hr (pH 6.1; Dako #S1699) and washed with PBS. The tissues were treated with 3% hydrogen peroxide for 12 min, and washed again in PBS. Retinas were immunostained using the peroxidase-based technique described above, with primary mouse anti-human A β mAb clones 12F4 or 6E10. To ensure that the component detected in the tissue was not derived from the exogenous normal serum, the blocking step was omitted for a subset of retinal tissues. The antibody was omitted from adjacent sections as an immunocytochemical control. Some of the immunostained sections were micro dissected and prepared for electron microscopic analysis. After treatment with osmium tetroxide/potassium ferricyanide, sections were infiltrated with epon/araldite resin and embedded between two acetate sheets, thin sectioned at 70 to 90nm in thickness, collected on copper grids, and lightly contrasted with Reynold's lead stain. The sections on grids were then analyzed on a JEOL JEM-2100 LaB6 TEM at 80 kilovolts (JEOL USA, Peabody, MA.). Images were captured on a Gatan SC1000 Orius CCD camera (Gatan Inc., Pleasanton, California).

Mice. For the analysis of curcumin absorption into the blood and brain, adult wild type C57BL/6 mice (n=20, females and males in equal numbers) were used. For in vivo retinal curcumin imaging studies, adult double-transgenic B6.Cg-Tg(APP_{swe},PSEN1_{dE9})85Dbo/Mmjax mouse models (MMRC stock #: 34832-JAX) ADtg mice and their non-transgenic littermates were used (total of n=24; females and males in equal numbers between the age of 9 and 11 months old).

Curcumin formulation bioavailability into the blood and brain in wild type mice. Curcumin absorption into the blood and brain was assessed after feeding wild type C57BL/6 mice (n=5 per group) several commercially available curcumin formulations (e.g. Sabinsa Corporation, Acros Organics, Longvida® Optimized Curcumin; 2000 parts per million in Chow) or phosphatidylcholine (PC) in Chow (vehicle) for 14 days (Supplemental Figure 4A). At the end of the experiment, mice were anesthetized with a lethal dose of pentobarbital (100 mg/kg bw). After blood collection, mice were perfused with non-fixative buffer to remove blood from the brain, and curcumin was measured by HPLC (Supplemental Figure 4B) and as previously described(5, 6).

Blood Collection. After exposing the heart cavity, blood was collected from the left ventricle of anesthetized subjects into EDTA tubes. Blood was centrifuged at 2000x g at 4°C for 15 min, separated into RBC and plasma fractions, and then snap frozen in dry ice. Acetic acid was added to blood prior to extraction to minimize degradation during ethylene acetate extraction. In comparison to neutral pH, acidic pH was found to minimize curcumin's ex vivo degradation to its metabolites (Supplemental Figure 7A).

Curcumin analysis. Curcumin was measured by high-performance liquid chromatography (HPLC)(6) or by LCMSMS(5) as previously described. The HPLC-MS/MS system consisted of an Agilent HPLC system (Hewlett Packard, 1090 series liquid chromatogram, USA) and a Sciex II FIA-ESI API 3000 tandem mass spectrometer (Biomolecular Mass analyzer/Applied Biosystems, USA). Curcumin was analyzed from negative ion in MRM mode. The analytical C18 HPLC column (Supelco ascentis express, 2.7 µm particle size, 150mm×2.1 mm, Supelco, Bellefonte, PA, USA) was used in the LC system. The gradient A mobile phase was a mixture of 10 mM ammonium acetate and gradient B was a mixture of 5 mM ammonium acetate in acetonitrile/isopropanol (50:50, v/v). Injection volume was 100 µl with run time of 50 min and flow rate of 0.1 ml/min. The sensitivity of multiple reactions monitoring (MRM) was optimized by testing an infusion of 1pg/ml of curcumin. We also confirmed background noise level by running the blank sample in between 10 consecutive samples. The background noise in the blank sample was not elevated in each consecutive period. Ion source gas, curtain gas, and collision gas flows were at instrument settings of 250, 120, and 65 psi, respectively. The declustering potential and

focusing potential were at 46 and 200V, respectively. The mass spectrometer was operated under MRM mode with collision energy of 24 eV. The m/z values of the specific transitions for curcumin were: 367.0, 148.7, 172.4, 216.3; tetrahydrocurcumin: 372.0, 193.5, 236.0; vanillin: 152, 93.2, 108.7, 136.4; hexahydrocurcumin: 374, 179.1, 193.1; octahydrocurcumin: 376, 122.2, 134.9; and for the internal standard, tetramethoxycurcumin: 396.4, 149.5, 297.1, 337.6. Linear regression was used to generate calibration curves from standards, and a standard was generated from ratio of curcumin to internal standard.

Optimization of oral curcumin formulation and regimen for retinal A β imaging in ADtg mice. Curcumin formulation, dose and regimen were tested through in vivo retinal imaging of curcumin fluorescence using ADtg mice and a Micron III retinal imaging microscope for rodents (Phoenix Research Laboratories, San Ramon, CA). Curcumin (diferuloylmethane; C₂₁H₂₀O₆) is a natural fluorochrome isolated from the rhizomes of *Curcuma longa* (turmeric) with high affinity to A β deposits. We previously studied its bioavailability to CNS tissues, following administration to peripheral blood, and its spectral properties when specifically bound to retinal A β deposits(7, 8). After assessing several curcumin formulations for oral administration, we chose Longvida® Optimized Curcumin due to its high bioavailability to blood and brain tissues and improved ability to detect retinal A β plaque in mice. To further select and calibrate the optimal oral curcumin formulation for clinical trials, we tested two forms of Longvida curcumin (water vs. lipid soluble) in vivo in 9-month-old ADtg mice using different regimens (Supplemental Figure 5C). Noninvasive retinal imaging was performed 24 h prior to curcumin administration, as well as 4-6 h and 1-3 days following oral curcumin (0.06-0.18 mg/gBW in mice, equivalent to 4, 8, 10, 12 gr/70Kg average human BW). The selected optimal curcumin for retinal amyloid imaging was the solid lipid curcumin nanoparticle (SLCP) Longvida® capsules (of which curcumin was >60%). This formula was previously reported to facilitate steady and extended transfer of curcumin into the bloodstream and CNS target tissues(9).

To further determine dosages, we tested high versus low Longvida curcumin (Supplemental Figure 5D-F). Retinas of 10.5-month-old ADtg mice (n=12; females and males at equal numbers) were imaged before and after oral gavage of SLCP Longvida curcumin. Three groups of four mice were administered different doses (0.1427mg/gBW/day, 1.142mg/gBW/day or PBS, for 2 days). The calculated equivalent in humans is 10g for low-dose Longvida curcumin and 80g for high-dose Longvida curcumin.

Noninvasive retinal amyloid imaging in animal models. Mice were anesthetized with ketamine and dexdomitor. Following the imaging, mice were injected with Antisedan (atipamezole) for reversal of the sedative and analgesic effects of dexdomitor. Care was taken to keep anesthetized animals warm throughout the procedure. Mouse pupils were dilated to about 2 mm diameter with 0.5% phenylephrine hydrochloride ophthalmic solution (Bausch & Lomb, Rochester, NY) combined with 0.5% tropicamide ophthalmic solution (Mydral, Bausch&Lomb). Mouse eyes were covered with imaging solution lubrication drop, which served as an optical coupling medium and preserved the eye's moisture, to facilitate longer and repeated live retinal imaging. Retinas were imaged in vivo using the Micron III microscope with identical light exposure time and intensity (gain and shutter modes). The Micron III microscope was adjusted to visualize fluorescent signals at high resolution and equipped with a 3-CCD camera (1000 to 1 dynamic range and 30 frames per second output at XGA resolution) and a specific set of filters suitable for detecting curcumin fluorescence. Images and videos of the retina were repeatedly captured at several angles to visualize a larger retinal field and eliminate non-specific reflection signals. Images were exported to ImageJ 1.46r (NIH program) to calculate increased curcumin fluorescent intensity in A β plaques (n=5 deposits for each retina from identical regions, relative to background area).

Noninvasive retinal amyloid imaging in live human subjects. Patients with clinical diagnosis of mild to moderate AD were included based on criteria from The National Institute of Neurological and Communication Disorders, and The Alzheimer's Disease and Related Disorders Association for staging of dementia in AD, using the MMSE scoring system (scores of 12-23, Supplemental Table 2). Absence of cognitive dysfunction was ascertained in controls. Controls were asymptomatic individuals with no

evidence for memory or cognitive executive impairment according to self-reporting and/or family members and exhibit no deficit in activity of daily living (ADL). For the clinical trials, 16 subjects participated, of which 10 were AD patients and 6 were healthy controls (Supplemental Table 2). These 16 subjects were included in the quantitative retinal amyloid analysis. In addition, two cognitively normal individuals with dry AMD diagnosis and lack of cognitive impairment were included in our study; for more details see Supplemental Figure 8.

Pilot clinical studies have used a variety of ophthalmic imaging devices in order to test imaging resolution, excitation wavelength, data collection frame rates, and usability/patient comfort differences. The images in Figure 6-7 were captured with the Heidelberg Spectralis HRA scanning laser ophthalmoscope at 488nm excitation (Heidelberg, Germany), and were obtained after an extended period of imaging. The images in Figure 8 were obtained using the Optos Optomap Tx (Optos, UK) in high-resolution mode. The Optos provided a wide field image with uniform focus. A subset of patients was imaged using the Nidek F10 in high-resolution mode and 488nm excitation. Nidek F10 provided high spatial resolution with ability for wide field and relatively short exposure times to obtain multiple retinal images (Supplemental Figure 6D-G).

Exclusion criteria for clinical trials were: 1) patients with major cognitive impairment not due to AD (i.e. evidence of brain damage, including significant trauma, stroke, hydrocephalus, lacunar infarcts, seizures, mental retardation, or serious neurological disorder), 2) history of alcoholism or drug abuse within the past year, 3) a score greater than 4 on the Modified Hachinski Ischemia Scale, indicative of cerebrovascular disease, 4) systemic illness that could influence patient safety and protocol compliance (e.g. severe hepatic, renal, cardiovascular, or metabolic diseases), 5) corticosteroid uptake within the past 30 days or during the study, 6) patients with current or previous bile duct obstruction, gallstones, or gastrointestinal disorders, 7) pregnancy or breast feeding, and 8) for AD patients and controls, posterior pole ocular pathology, such as AMD and optic neuropathies, including open-angle high intraocular pressure glaucoma. In addition, we excluded 10 subjects from the study due to poor image quality, low

dosing of curcumin, withdrawn consent, or image artifacts. As mentioned above, we also imaged two cognitively normal individuals with dry AMD diagnosis and lack of cognitive impairment or any other adverse physical condition (see Supplemental Figure 8).

Phantom eye model and ophthalmic device development. A model eye was developed to provide a standardized comparison between retinal imaging devices and to test device modifications. The model eye used was the optical equivalent of a live human eye, retrofitted with various targets representing the retina. One such adaptation consisted of fluorescent micro-beads with specific peak fluorescence. Based on prior analyses in transgenic mice and human cadavers, we determined the target peak fluorescent wavelength of curcumin. The model eye was positioned on the Heidelberg Spectralis, Topcon 50DX, Optos Optomap Tx, and Nidek F10 fundus imaging devices to generate test images to compare fluorescence among devices. The model eye was used throughout the trials to evaluate overall performance of a variety of devices at the desired wavelength.

Our initial studies using a variety of ophthalmic imaging instruments, including scanning laser ophthalmoscopes (SLO) and fundus cameras, showed that the confocal laser-based devices provide better spatial resolution when imaging fluorescent plaques. The SLO used for this study provided laser excitation at 488 nm and 532 nm and can generate a suitable fluorescent emission image. Approximate pixel size on the retina is 6 μm . Several SLO devices were successfully modified to allow a wide-angle view of the retina and installed suitable emission filters to capture curcumin-specific fluorescent signals. We determined optimal illumination intensity and number of frames necessary to form a suitable image. We first tested each device with phantom eyes. Patients and healthy controls were enrolled for regimen and imaging methodology optimization, and an imaging protocol for the subsequent imaging trial was determined.

Curcumin administration in human subjects. A dose of 4 grams of Longvida® Solid-Lipid Curcumin Particle containing 1 gram of curcumin was mixed with Hunt's Snack Pack Pudding and taken once a day

for several days prior to retinal imaging. A non-biased witness observed each patient take his/her daily dose of Longvida curcumin (4 g/per day). Curcumin dose and imaging session schedule were determined based on initial imaging tests and pharmacokinetics.

Following informed consent, patients underwent a series of tests, including slit lamp ophthalmic exam, binocular indirect ophthalmoscopy, blood draw for curcumin, liver and kidney panel, height, weight, and BMI measurement, Snellen visual acuity, color fundus photography, red-free imaging, autofluorescence imaging, optical coherence tomography, and curcumin fluorescence imaging. Patients were asked to take, or continue taking, a standard over the counter oral vitamin E supplement (which increases curcumin absorption) beginning at baseline and continuing through day 4. The final dose of curcumin was taken approximately 4 h prior to curcumin fluorescence imaging procedure.

Curcumin pharmacokinetics in humans. Plasma and RBC curcumin samples from 6 subjects were collected 4 and 7 h post-dosing on Days 0, 1, 3, 10 and 30. Samples were analyzed by LCMSMS as previously described(5). Data from one subject were excluded from analysis due to extremely large concentrations reported (some > 100-fold above the mean values). Concentrations at 4 h post-dosing for each day were generally greater than 7 h sampling time, though 7 h curcumin exposure was within 2-fold, suggesting a relatively constant exposure between 4 and 7 h. Curcumin exposure variation was large (>60% CV) at most time points sampled.

Mean maximal plasma curcumin concentrations ranged from 15.1 nM on Day 0 to 455 nM on Day 10 showing approximately 30-fold accumulation. A 1-compartment pharmacokinetic model was fit to the data. Despite insufficient data for a more complex model fit, the model was adequate for interpretation. Clearance (CL) was estimated at 1.02 L/h with relatively poor precision (65% RSE). Volume (V) and absorption rate constant (k_a) were estimated at 852 L and 0.146 (1/h), respectively. V and k_a were estimated with moderate precision, 18% RSE and 38% RSE, respectively. Inter-individual variability was large for CL. The observations are qualitatively similar to data previously reported using this Longvida formulation(9).

Imaging protocol. Many factors influence the quality of images used to identify and quantify fluorescent spots in the retina. The protocol for the Optos Optomap Tx instrument involves collecting, aligning, and averaging at least four images of each region to improve signal-to-noise ratio (SNR). The images are collected sequentially while the patient is positioned at the instrument with a constant gaze so that retinal region images are approximately the same. This enables the automatic image registration algorithm to correct for translation, rotation, and image warping. Small movements between each frame minimize any scan line artifacts. Both patient's eyes were imaged at three field positions (central, superior, and inferior). For each field, 4 frames were collected (12 images per eye).

Images were excluded from analysis for a variety of reasons including: 1) retinal structures out of focus throughout image, 2) eye movement causing feature distortion or motion blurring, 3) significant obstructions blocking view of the retina (e.g. eye lashes, blinking, or floaters that cast shadows on the image), 4) severe image warping causing distortion of retinal features, 5) insufficient number of suitable frames to align and average, 6) reflections and other illumination artifacts that may cause stripes or rings, 7) insufficient periphery view (optic disk should be at the very top/bottom of inferior/superior frame), and 8) cataracts and other lens abnormalities that may prevent high-resolution imaging.

At this time, the image quality of the unaligned baseline and the curcumin image are assessed by calculating the multi-scale gradient and determining the standard deviation of the result. A value less than 2.0 is considered low quality, as the resulting analysis may be inaccurate (typically caused by blur, haze, or movement in the image).

Semi-automated and fully automated image analysis. Initial analysis of the Heidelberg retinal images was achieved by manually identifying the same spots in both the Baseline and Curcumin images and measuring their intensities. The manual analysis was necessary to validate the increase in spot fluorescence intensity; however, going forward this approach would be neither efficient nor unbiased.

The second version of the RAI analysis was designed to automate the process of identifying areas of peak fluorescence intensity on contrast-normalized images and to calculate RAI score (currently in arbitrary units). Comparing the ratio of RAI values between Day 10 and Baseline, there is an approximate 2- to 3-fold increase in RAI value. This results from stronger fluorescence intensities and more objects detected. In automating the analysis of Optos datasets, only spots of a specific morphology that increase in overall fluorescence intensity compared to the baseline were considered A β plaques and thus included in RAI scoring. This was done to eliminate possible bright retinal structures not related to curcumin dosing. The RAI algorithm was modified to account for density of detected spots and scoring was normalized by retinal area analyzed.

After the Baseline image was aligned to the Curcumin image, a population of spots was detected in the Curcumin image, and intensity and area statistics for each spot were calculated. The same spot mask was applied to the Baseline image and the same statistics were calculated. The total fluorescence intensity contained in each Baseline spot was plotted against the corresponding Curcumin spot. Only those curcumin spots, which were sufficiently brighter than Baseline image spots were retained, based on the assumption that they were above noise variations. The image processing steps involved conversion of raw retinal images into RAI score. The images were selected and aligned with background images, and calculations of RAI scores were fully automated (Figure 8). The ‘edges’ in the image were identified by a multi-resolution gradient calculation using a Gaussian pyramid, which enabled identification of punctate plaques while ignoring the more diffuse autofluorescence that was also present. The gradient calculation also identified the sharp edges of the retinal vessels, which were masked out during analysis.

Calculation of retinal amyloid index (RAI) score. The RAI score for each region image encompasses a number of factors that characterize the detected spot number, area, intensity, and distribution. Exact RAI formulation is considered confidential and a trade secret. We display RAI scores and spot number calculated from predefined eye and retinal region (superior quadrant). Alzheimer's patients occasionally

have some regions relatively clear of spots and other regions containing more. We observed that A β plaques appeared in clusters in some but not in all regions of postmortem retinas from AD patients.

Optical coherence tomography (OCT). High definition OCT scans were performed with Heidelberg Spectralis on selected test subjects with large plaques to ascertain retinal layer location of plaques. The OCT scans of several test areas show that spots appear above the RPE and therefore cannot be classic drusen associated with age-related macular degeneration (AMD).

Statistics. GraphPad Prism 6.01 (GraphPad Software) was used for analysis. A comparison of three or more groups (days of blood sampling) was performed using one-way ANOVA followed by a Bonferroni or Tukey's multiple comparison posttests of paired groups. Logarithmic transformation Analysis of Covariance (ACNOVA) was also applied for PK data analysis. Two-group comparisons were analyzed using a two-tailed unpaired student t-test. The statistical association between two or more variables was determined by Pearson's correlation coefficient (r) test (GraphPad Prism). Pearson's r indicates direction and strength of the linear relationship between two variables. Results are expressed as means \pm standard errors of the mean (SEM). p values less than 0.05 are considered significant.

Study approval. All human participants provided written approval of the protocol and informed consent. Clinical trials were approved by external review committee Quorum Review (Seattle, WA; IRB00003226) and by the U.S. Department of Health and Human Services (HHS) for the Protection of Human Subjects for Institutions within the United States (Federalwide Assurance #: FWA00019841).

Studies with live mice. For the curcumin bioavailability study, mice procedures were undertaken according to regulations of the Division on Laboratory Animal Medicine (DLAM) at the University of California - Los Angeles under an approved protocol. Live imaging experiments in ADtg mice were conducted according to regulations of the Cedars-Sinai Medical Center Institutional Animal Care and Use Committee (IACUC) under an approved protocol.

References:

1. Mirra SS, et al. The Consortium to Establish a Registry for Alzheimer's Disease (CERAD). Part II. Standardization of the neuropathologic assessment of Alzheimer's disease. *Neurology*. 1991;41(4):479-486.
2. Hyman BT, et al. National Institute on Aging-Alzheimer's Association guidelines for the neuropathologic assessment of Alzheimer's disease. *Alzheimer's & dementia : the journal of the Alzheimer's Association*. 2012;8(1):1-13.
3. Ichihara K, Uchihara T, Nakamura A, Suzuki Y, and Mizutani T. Selective deposition of 4-repeat tau in cerebral infarcts. *Journal of neuropathology and experimental neurology*. 2009;68(9):1029-1036.
4. Uchihara T. Silver diagnosis in neuropathology: principles, practice and revised interpretation. *Acta neuropathologica*. 2007;113(5):483-499.
5. Begum AN, et al. Curcumin structure-function, bioavailability, and efficacy in models of neuroinflammation and Alzheimer's disease. *The Journal of pharmacology and experimental therapeutics*. 2008;326(1):196-208.
6. Heath DD, Pruitt MA, Brenner DE, and Rock CL. Curcumin in plasma and urine: quantitation by high-performance liquid chromatography. *J Chromatogr B Analyt Technol Biomed Life Sci*. 2003;783(1):287-295.
7. Koronyo Y, Salumbides BC, Black KL, and Koronyo-Hamaoui M. Alzheimer's disease in the retina: imaging retinal abeta plaques for early diagnosis and therapy assessment. *Neuro-degenerative diseases*. 2012;10(1-4):285-293.
8. Koronyo-Hamaoui M, et al. Identification of amyloid plaques in retinas from Alzheimer's patients and noninvasive in vivo optical imaging of retinal plaques in a mouse model. *Neuroimage*. 2011;54 Suppl 1(S204-217).
9. Gota VS, et al. Safety and pharmacokinetics of a solid lipid curcumin particle formulation in osteosarcoma patients and healthy volunteers. *J Agric Food Chem*. 2010;58(4):2095-2099.